International Journal of Extreme Manufacturing

Programmable mechanical properties of additively manufactured novel steel

OPEN ACCESS
IOP Publishing | IMMT
International Journal of Extreme Manufacturing
Int. J. Extrem. Manuf. 7 (2025) 015001 (18pp)
https://doi.org/10.1088/2631-7990/ad88bc

Programmable mechanical properties of additively manufactured novel steel

Jinlong Su[1,2], Qian Li[3], Jie Teng[2], Fern Lan Ng[1], Zheling Shen[4], Min Hao Goh[1], Fulin Jiang[2], Swee Leong Sing[5], Tao Yang[3] and Chaolin Tan[1,*]

[1] Singapore Institute of Manufacturing Technology (SIMTech), Agency for Science, Technology and Research (A*STAR), Singapore 636732, Singapore
[2] College of Materials Science and Engineering, Hunan University, Changsha 410082, People's Republic of China
[3] Department of Materials Science and Engineering, City University of Hong Kong, Hong Kong Special Administrative Region of China, People's Republic of China
[4] School of Materials Science & Engineering, University of Science and Technology of China, Shenyang 110016, People's Republic of China
[5] Department of Mechanical Engineering, National University of Singapore, Singapore 117575, Singapore

E-mail: tclscut@163.com and tan_chaolin@simtech.a-star.edu.sg

Received 21 April 2024, revised 6 July 2024
Accepted for publication 18 October 2024
Published 5 November 2024

Abstract

Tailoring thermal history during additive manufacturing (AM) offers a feasible approach to customise the microstructure and properties of materials without changing alloy compositions or post-heat treatment, which is generally overlooked as it is hard to achieve in commercial materials. Herein, a customised Fe–Ni–Ti–Al maraging steel with rapid precipitation kinetics offers the opportunity to leverage thermal history during AM for achieving large-range tunable strength-ductility combinations. The Fe–Ni–Ti–Al steel was processed by laser-directed energy deposition (LDED) with different deposition strategies to tailor the thermal history. As the phase transformation and *in-situ* formation of multi-scale secondary phases of the Fe–Ni–Ti–Al steel are sensitive to the thermal histories, the deposited steel achieved a large range of tuneable mechanical properties. Specifically, the interlayer paused deposited sample exhibits superior tensile strength (∼1.54 GPa) and moderate elongation (∼8.1%), which is attributed to the formation of unique hierarchical structures and the *in-situ* precipitation of high-density η-Ni_3(Ti, Al) during LDED. In contrast, the substrate heating deposited sample has an excellent elongation of 19.3% together with a high tensile strength of 1.24 GPa. The achievable mechanical property range via tailoring thermal history in the LDED-built Fe–Ni–Ti–Al steel is significantly larger than most commercial materials. The findings highlight the material customisation along with AM's unique thermal history to achieve versatile mechanical performances of deposited materials, which could inspire more property or function manipulations of materials by AM process control or innovation.

* Author to whom any correspondence should be addressed.

2631-7990/25/015001+18$33.00

Supplementary material for this article is available online

Keywords: additive manufacturing, directed energy deposition, thermal history control, microstructure control, mechanical property programming, materials customisation, *in-situ* precipitation

1. Introduction

Additive manufacturing (AM) is a cutting-edge manufacturing technology with the remarkable ability to fabricate intricate and high-performance net-shaped metallic components [1, 2]. The distinctive characteristic of AM lies in its unique layer-by-layer deposition approach, wherein materials are rapidly melted, solidified, and cooled, followed by intrinsic thermal cycling [3–5]. The rapid solidification and cooling of AM ensure that ultrafine-grained microstructure with supersaturated solid solution atoms can be obtained, while the intrinsic thermal cycling endows an *in-situ* heat treatment, inducing *in-situ* precipitation (e.g. η-Ni_3Ti in AM of Fe–19Ni–5Ti [6] and β'-NiAl in AM of Fe–19Ni–*x*Al [7]) or *in-situ* decomposition of metastable phases (e.g. martensite decomposition in AM of Ti–6Al–4V alloy [8]) during AM. These process characteristics enable the *in-situ* tailoring of microstructure and property, and the *in-situ* microstructural evolutions associated with the unique thermal history play a major role in shaping the performance of AM-built components.

In laser AM, adjusting laser power, scan speed, hatch spacing, or layer thickness can alter the thermal history significantly [9, 10]. However, changing these energy-related process parameters will affect the densification of AM-built materials, which overshadows the effects of thermal history on mechanical properties [11]. Differing from the energy-related parameters, the interlayer paused time emerges as a crucial AM process parameter for shaping thermal history without affecting the densification of deposited materials [12]. The interlayer paused time can affect the net thermal build-up to tailor thermal history in the deposited material for microstructural control [6, 13]. Specifically, using a short interlayer paused time can increase the thermal accumulation, thereby promoting the *in-situ* heat treatment effects, while using a long interlayer time can inhibit thermal accumulation and ensure a high thermal gradient and cooling rate in the whole building. As an example, Kürnsteiner *et al* [6] reported that the degree of martensitic transformation of the laser-directed energy deposition (LDED)-built Fe–19Ni–5Ti maraging steel heavily relies on the interlayer paused time due to the different heat build-up during LDED, and the intrinsic thermal cycling of LDED induced the *in-situ* precipitation of η-Ni_3Ti phase [7, 14].

Apart from adjusting process parameters, external heating/-cooling is also a feasible solution to tailor the AM thermal history [15]. Substrate heating is a widely implemented auxiliary technique for metal AM and has been incorporated into numerous commercial AM systems [16]. Benefiting from the heated substrate, the temperature gradient and cooling rate can be reduced simultaneously, hereby alleviating residual stress and crack sensitivity [17, 18]. Meanwhile, substrate heating can also affect the phase transformation behaviour and microstructural formation. For materials with martensitic transformation (e.g. maraging steels, $(\alpha + \beta)$-Ti alloys), reducing thermal gradient and cooling rate can retard the martensitic transformation [19]. Heating the substrate to a temperature above the martensite start temperature can even inhibit the martensitic transformation during AM, significantly affecting the microstructure and properties of the deposited materials [16, 20].

As discussed above, the thermal history control in AM enables *in-situ* microstructural tailoring, which could be performed to achieve versatile mechanical performances without adjusting alloy composition and exerting time-consuming post-heat treatments. However, up until now, the full potential of the AM process characteristics on microstructure tailoring remains largely undiscovered. This is because most commercial powder feedstocks used for AM are predominantly designed for conventional manufacturing routes (e.g. casting and forging), which hardly cater to the metallurgical characteristics of AM (i.e. rapid solidification/cooling rate and intrinsic cyclic thermal inputs [21]). As a result, the mechanical properties of commercial materials are hard to tailor by controlling thermal history due to the lack of rapid precipitation kinetics. Under this circumstance, post-heat treatments are generally needed for AM-built materials to improve their mechanical performance. For instance, direct-aging or solution-aging treatments are necessary for AM-built commercial C300 maraging steel to form high-density precipitates and enhance mechanical strength [22]. However, the additional post-heat treatment inevitably compromises the time and energy efficiency of AM. The potential of leveraging thermal history during AM to achieve large-range strength-ductility combinations in the AM-built materials without post heat treatment or changing alloy composition is generally overlooked. AM-built materials with large-range tunable mechanical properties can meet various applications, which reduces storage load and extends the material's application range significantly. This can potentially revolutionise the AM field by harnessing the full capabilities of thermal history control in tailoring microstructure and property directly, thus propelling the technology towards more streamlined and efficient industrial applications.

Presented here are our latest research findings on leveraging thermal history of AM for achieving large-range tunable strength-ductility combinations in an LDED-built novel Fe–Ni–Ti–Al maraging steel without post-heat treatment or changing alloy composition. The thermal history was tailored by

interlayer paused strategy and implementing external heating/-cooling during LDED. The effects of thermal histories tailoring on the microstructural formation, mechanical properties, and strengthening and toughening mechanisms of the novel Fe–Ni–Ti–Al maraging steel are elucidated.

2. Materials and methods

2.1. Material and LDED process

In this work, a novel Fe–Ni–Ti–Al maraging steel characterised by rapid precipitation kinetics is adopted as the feedstock. The compositions and particle size distributions of the raw powder are summarised in table 1. The proper addition of Ni (21.1 wt%) improves the stability of austenite and ensures the transformation into martensite upon cooling from the austenite phase, which is crucial for the subsequent aging process that significantly enhances the mechanical strength. Ti in conjunction with Ni facilitates the rapid precipitation of η-Ni_3Ti during AM, enhancing the hardening response of the steel. Additionally, Al is used to decrease the density and improve the oxidation resistance of the steel. The martensitic start temperature (M_S) of the Fe–Ni–Ti–Al steel is ∼182 °C as measured by a dilatometer (as shown in figure S1), indicating that the martensitic transformation is highly sensitive to thermal history during LDED [23]. The electron backscatter diffraction (EBSD) images and energy dispersive x-ray spectroscopy (EDX) mappings of the Fe–Ni–Ti–Al raw powder are presented in figures 1(a)–(e), respectively. The raw powder mainly consists of martensite, austenite, and minor Ti_2Ni Laves phases. The EDX mappings in figure 1(e) indicate that the austenite phase is rich in Ni and Ti since Ni and Ti both act as austenite stabilisers in the current steel [6].

Single tracks, single layers, and block samples were printed to optimise the LDED process parameters. The parameters were fine-tuned within a laser power range of 700–1000 W and a scan speed range of 900–1800 mm·min^{-1}. The printing process incorporated a raster scanning strategy that involved rotating each layer by 90°. The powder feed rate is fixed at 2.3 g·min^{-1} to ensure great deposition quality with moderate deposition efficiency. The distance of the nozzle to the substrate is kept at 9 mm. The deposited block size is 75 mm × 50 mm, and a mild steel plate is used as the substrate. Notably, a novel experimental setup is designed to tailor the thermal history of LDED, as shown in figure 1(f). Specifically, a heating plate and a cooling plate are both installed under the substrate to serve as the heating and cooling source, respectively. The image of the experimental setup is shown in figure S2. The thermal history is recorded by a K-type thermocouple placed at the edge of the 1st printed layer because the minimum temperature of the built can be determined by measuring the temperature of this location (figure 1(f)). Four types of deposition strategies, including common continuous deposition (CCD), interlayer paused deposition (IPD), constant heating deposition (CHD), alternated heating deposition (AHD), are adopted to tune the thermal histories during LDED of Fe–Ni–Ti–Al steel: (i) CCD involves the continuous layer-by-layer printing without interlayer pauses, representing the most commonly adopted deposition strategy; (ii) IPD incorporates a 100 s interlayer pause to curtail thermal accumulation during LDED, ensuring the uniformity of martensitic transformation across the entire built; (iii) CHD maintains the substrate temperature at 200 °C, without interlayer pauses during deposition, ensuring that the solidified material remains above the *Ms* of the Fe–Ni–Ti–Al steel during printing. This process suppresses martensitic transformation during printing and alters the microstructure accordingly; (iv) AHD employs heating and cooling plates alternately between layers to craft a hierarchically structured steel. During AHD, the initial layer is printed with the substrate heated to 200 °C, followed by water cooling using a cooling plate; after that, shifting to the next layer printing at room temperature (without substrate heating), alternatingly layer-by-layer until the entire block is printed.

2.2. Microstructural characterisation and mechanical testing

The optical microscope (OM) was adopted to characterise the macro-structure of the as-built samples. The metallographic specimens were cut from the *X*–*Z* plane. The phase composition was determined using x-ray diffraction (XRD), with the tests conducted at a step size of 0.02° and a scan rate of 1 step·s^{-1}. The volume fractions of face-centred cubic/body-centred cubic (fcc/bcc) phases were estimated by the integrated intensities of the $(111)_{fcc}$ and $(110)_{bcc}$ as follows [24]:

$$V_{bcc} + V_{fcc} = 1 \tag{1}$$

$$V_{fcc} = (a \times I_{fcc}) / (a \times I_{fcc} + I_{bcc}) \tag{2}$$

where V_{bcc} and V_{fcc} are the volume fraction of bcc and fcc phases, respectively. I_{bcc} and I_{fcc} are the integrated intensities of $(111)_{bcc}$ and $(110)_{fcc}$ peaks, respectively. When the $(111)_{bcc}$ and $(110)_{fcc}$ peaks are taken into consideration, the proportional constant a is estimated to be 1.4, according to Tanaka and Choi's work [24]. Although the integral tensity method assumes that the grain is randomly orientated and the effect of the texture is neglected, herein, the integral tensity method is still considered as an effective method for comparing the phase fraction, considering that the texture of all the deposited alloys is similar.

EBSD tests were conducted on an Oxford detector operating at 20 kV using a step size of 100 nm, and the EBSD data were analysed using AZtecCrystal software. Samples for transmission electron microscope (TEM) analysis were taken from the steel using the FEI Scios dual-beam focused ion beam (FIB). Subsequently, the multi-scale secondary phases and precipitates were characterised using the TEM via selected area electron diffraction (SAED), scanning TEM (STEM), high-resolution TEM (HRTEM), and high-angle annular dark field (HAADF) STEM techniques. Needle-shaped specimens for atom probe tomography (APT) were prepared using lift-outs and annular milling with an FEI Scios FIB/scanning electron microscope. APT characterisations were conducted using a CAMECA LEAP 5000 XR

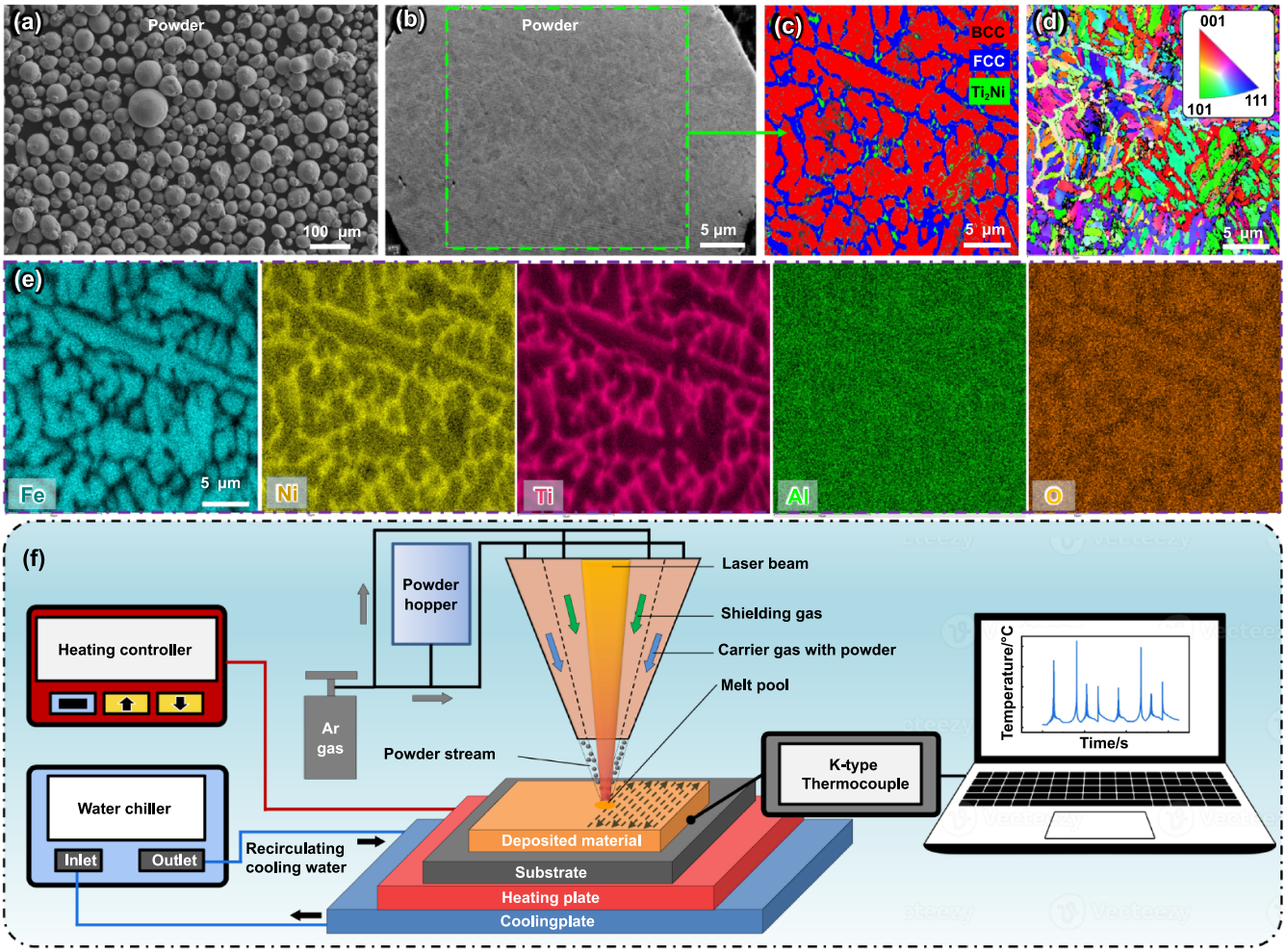

Figure 1. Materials and methods. (a)–(e) EBSD images and EDX mappings of the Fe–Ni–Ti–Al raw powder, (f) schematic of LDED with heating and cooling plates, and the corresponding (e) experimental setup.

Table 1. Composition and size distribution of the raw Fe–Ni–Ti–Al maraging steel powder.

Composition (wt%)						Size distribution (μm)		
Ni	Ti	Al	O	C	Fe	D_{10}	D_{50}	D_{90}
21.1	6.3	1.3	0.024	0.012	Bal.	26	37	55

local electrode atom probe. For three-dimensional reconstructions and subsequent data analysis, AP Suite 6.1 software was employed.

The mechanical properties of the LDED-built steels were evaluated via tensile and hardness tests. Tensile specimens were cut along horizontal directions (i.e. from the *X*–*Y* plane) with gauge dimensions of 26 mm × 6 mm × 3 mm, and tested by an Instron 5982 machine using a 20 mm extensometer. The loading speed of the tensile tests is 1 mm·min^{-1}. Microhardness testing was conducted using a Vicker hardness tester, employing a force of 100 gf and a hold time of 15 s. Additionally, the phase transformation and elemental segregation behaviours of the steel during LDED were analysed using the Thermo-Calc software with the TCFE9 database.

3. Results

3.1. Process developments

3.1.1. Processing parameters optimisation. To optimise the LDED process parameters for the Fe–Ni–Ti–Al steel, the relationships between processing parameters and track width were developed through the single-track deposition. As shown in figures S3(a)–(c), the track width became larger with increasing laser power under a constant scan velocity (1200 mm·min^{-1}), while under the same laser power (925 W), the track width became narrower with increasing scan velocity, as shown in figures S3(d)–(f). The track width over a wide range of laser processing parameters was about 1.2–1.4 mm. Considering a reasonable overlap rate of 40%–60% between

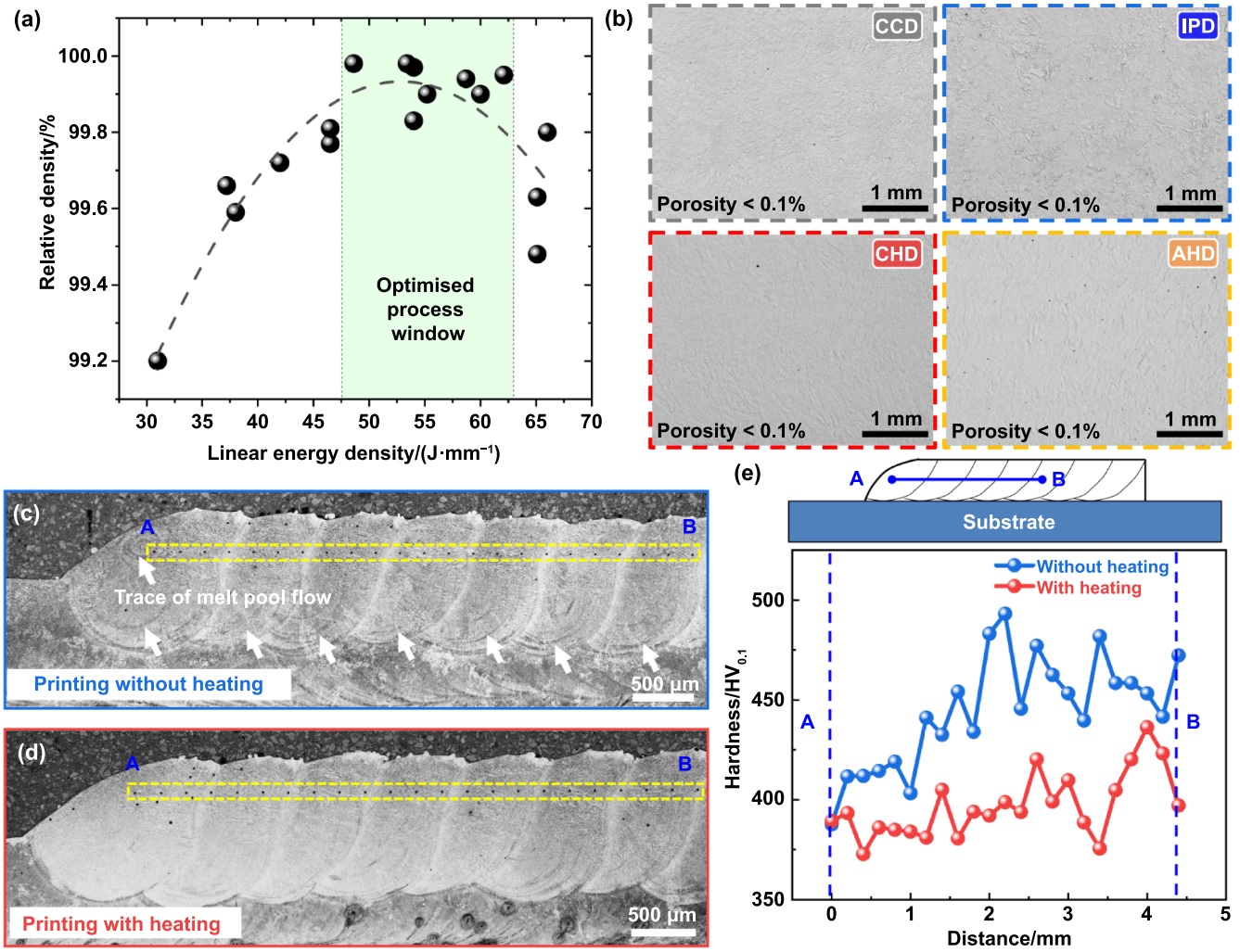

Figure 2. LDED process optimisation and single-layer deposition. (a) Relative density versus linear energy density, (b) OM of the CCD, IPD, CHD, and AHD cubic block samples, (c) single-layer printing without heating, (d) single-layer printing with heating (substrate temperature of 200 °C, scan movement from B to A), and (e) hardness distributions in the single-layer with and without substrate heating.

adjacent tracks, the hatch space was fixed as 0.65 mm in the following process parameters optimisation steps.

Next, the Fe–Ni–Ti–Al steel block samples were fabricated over a wide range of linear energy density via varying laser power and scan speed for optimising processing parameters. The powder feed rate was fixed at 2.3 g·min^{-1}, and the hatch spacing was fixed at 0.65 mm. The linear energy density E_L (J·mm^{-1}) is calculated as E_L = (laser power P)/(laser scan speed V). As shown in figure 2(a), the proper linear energy for the Fe–Ni–Ti–Al steel is determined to be 48–63 J·mm^{-1}. Insufficient laser energy could result in a lack of fusion, while excessive energy input could lead to material vaporisation and keyhole effect. Overall, the optimum laser power is determined to be 880–900 W, and the optimum scan speed is 900–1100 mm·min^{-1}. Under the optimised processing parameters (900 W and 1000 mm·min^{-1}), fully dense block samples (porosity $< 0.1\%$) can be obtained under various deposition strategies, as shown in figure 2(b). Note that the E_L used for fabricating the CCD, IPD, CHD, and AHD samples is the same, i.e. 54 J·mm^{-1}.

3.1.2. Material thermal sensitivity evaluation by single-layer deposition. Single-layer deposition experiments were carried out to analyse the sensitivity of mechanical properties to the thermal history of the Fe–Ni–Ti–Al steel. Without the multi-layer deposition and remelting, the effect of substrate heating on the mechanical properties can be revealed directly. Figures 2(c) and (d) present the single-layer printed with and without substrate heating, respectively. Notably, the trace of the melt pool disappears with substrate heating, which could be related to the reduced Marangoni convection since the substrate heating reduced the temperature gradient between the substrate and the melt pool. For the single-layer printed with substrate heating, the martensitic transformation is inhibited during printing since the substrate temperature (200 °C) is higher than the *Ms* (∼182 °C). Obviously, the hardness of the single-layer printed without heating is higher than that of the single-layer with heating (figure 2(e)). Besides, the single-layer printing without substrate heating exhibits a large hardness fluctuation, while the application of substrate heating leads to a more uniform hardness distribution across the

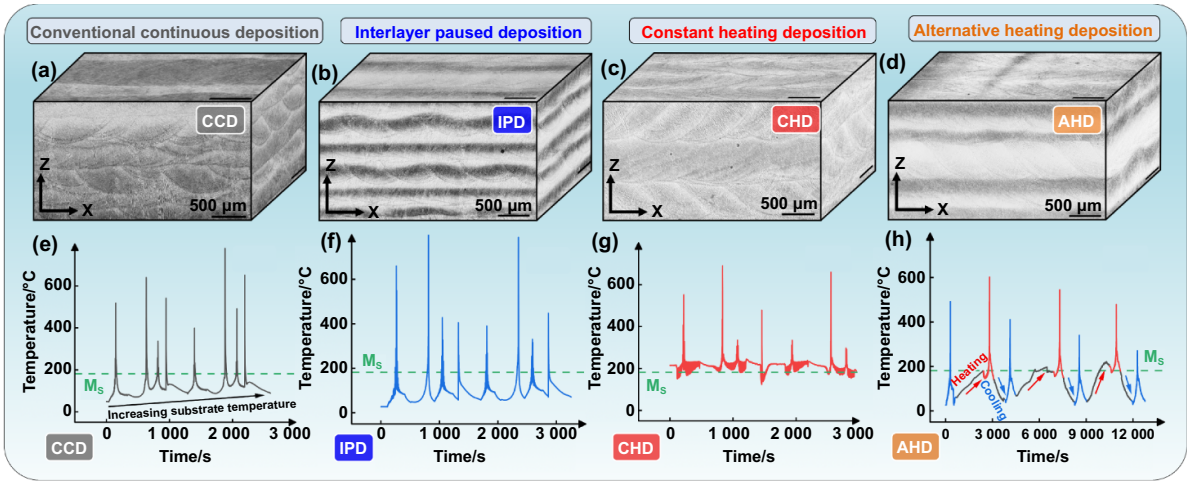

Figure 3. OM images and thermal histories of the LDED-built Fe–Ni–Ti–Al maraging steels under various deposition strategies. (a) and (e) CCD, (b) and (f) IPD, (c) and (g) CHD, (d) and (h) AHD.

single-layer (figure 2(d)), which could be attributed to the more consistent thermal history. Considering that the mechanical property of the Fe–Ni–Ti–Al steel is sensitive to the thermal history, various deposition strategies, including CCD, IPD, CHD, and AHD, are then utilised to tailor the mechanical property of the steel.

3.2. Microstructure tailoring via thermal history control

3.2.1. Macro-morphology observation and hardness mappings analysis. Figure 3 presents OM images and the corresponding temperature curves of the Fe–Ni–Ti–Al steel printed under various deposition strategies. For CCD, the substrate temperature increases gradually during printing. It can be inferred that the accumulated heat could partially inhibit the martensitic transformation (figure 3(a)). The CCD sample in figure 3(a) exhibits a uniform macrostructure, and the melt pool boundary is seen in the *X*–*Z* plane. For IPD, the temperature of the substrate was kept at about 50 °C–60 °C before printing each layer, ensuring the unity of martensitic transformation in the whole built (figure 3(b)). In the IPD sample, several parallel dark bands with a thickness of 100–200 μm were formed (figure 3(b)). The formation of dark bands is related to the high fraction of martensite caused by the local high cooling rate at the vicinity area of melt pool boundary and layer interface. For CHD, the martensitic transformation is inhibited during printing due to the higher substrate temperature (200 °C) compared to the *Ms* temperature of the steel (∼182 °C) (figure 3(c)). It can be inferred that all the martensite in the CHD sample forms during the cooling stage after printing and the cooling rate of the melt pool in CHD is more uniform compared to IPD. As a result, the CHD sample exhibits a bright, uniform macrostructure. In the case of AHD, the distinct alternating heating and cooling strategy leads to a layerwise structured macrostructure, as shown in figures 3(d) and (h). The appearance of dark bands on alternated layers of the AHD sample can be ascribed to the different thermal histories in adjacent layers. The macrostructure of the layer printed with substrate heating is similar to the CHD sample, while the layer printed without substrate heating is similar to the IPD sample.

The hardness mapping across several layers was conducted to further correlate the microstructure features with mechanical performance. The hardness distribution comparison between IPD and CHD samples is shown in figure 4. Notably, for the IPD sample, the hardness of the dark bands is about 100 HV higher than that of the bright region. The mechanisms for the relatively high hardness in these dark bands will be further characterised in the following sections. In contrast, the hardness of the CHD sample is distributed uniformly in the built, as shown in figures 4(d)–(f). Besides, the hardness of the CHD sample is relatively lower relative to the IPD sample (figure 4(g)), and it corresponds well with the single-layer printing experiments in figures 2(c)–(e). The hardness of the CCD sample (460–540 HV) is located between the IPD and CHD samples (see supplementary materials figure S4). Overall, these phenomena indicate that the phase transformation behaviour and mechanical property of the steel varies significantly under different deposition strategies.

3.2.2. Thermal history dependent phase constitutions. Figure 5 presents the IPF orientation and phase maps of the Fe–Ni–Ti–Al maraging steels printed under various thermal histories. There is no evident grain texture in these four samples, as observed in texture in figures 5(a)–(d). The epitaxial growth of grains across layer interfaces can be observed. For CCD and IPD printed steels, the bcc martensite phase tends to form at the melt pool boundaries. Considering the raw powder used for LDED is a pre-alloyed powder, the macro-scale phase inhomogeneity is unlikely to be caused by chemical segregation. As a result, the higher fraction of bcc at melt pool boundaries can be attributed to a higher cooling rate during solidification. The phase maps in figures 5(e)–(h) indicate that all the samples consist of a dual-phase (i.e. bcc

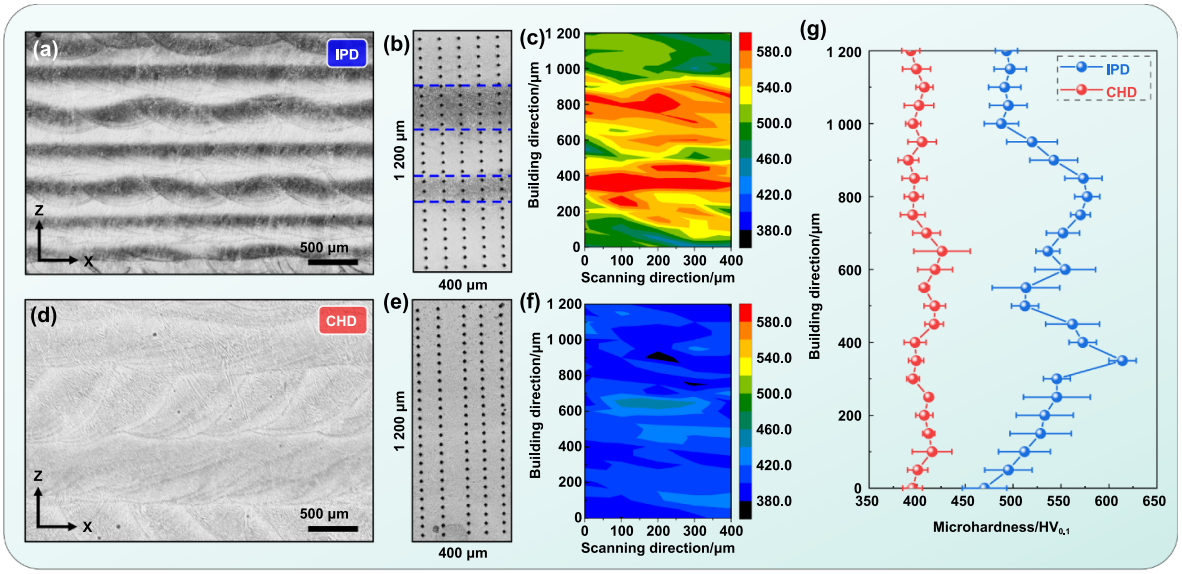

Figure 4. Hardness mappings of the IPD and CHD samples. (a)–(c) IPD sample, (d)–(f) CHD sample, (g) hardness distributions of IPD and CHD samples along the build direction.

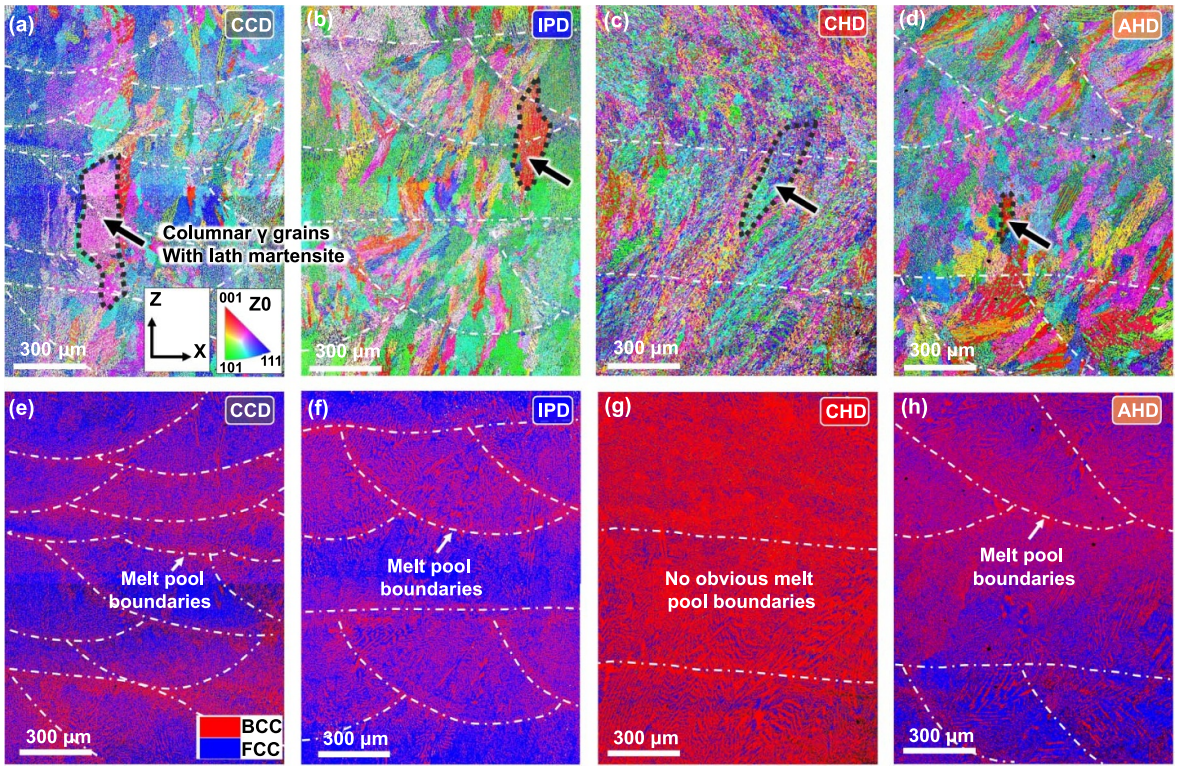

Figure 5. EBSD analysis of the LDED-built Fe–Ni–Ti–Al steels printed under various thermal histories. IPF orientation maps of the (a) CCD, (b) IPD, (c) CHD, (d) AHD samples, phase maps of the (e) CCD, (f) IPD, (g) CHD, and (h) AHD samples.

martensite + fcc austenite) microstructure, further evidenced by the XRD patterns presented in figure 6(a). According to the Schaeffler–Delong diagram [25], there unlikely exists ferrite, the high content of Ni (20.8 wt%) in this steel improved the stability of the fcc austenite phase, hereby inhibiting the transformation of austenite to ferrite. Moreover, the high cooling rate of the LDED process could also facilitate martensite formation.

The volume fractions of the fcc and bcc phases were estimated by the integrated intensities of the $(111)_{fcc}$ and $(110)_{bcc}$ of the XRD patterns, as elucidated in section 2.2. According to figure 6(b), the IPD sample has a higher bcc phase fraction

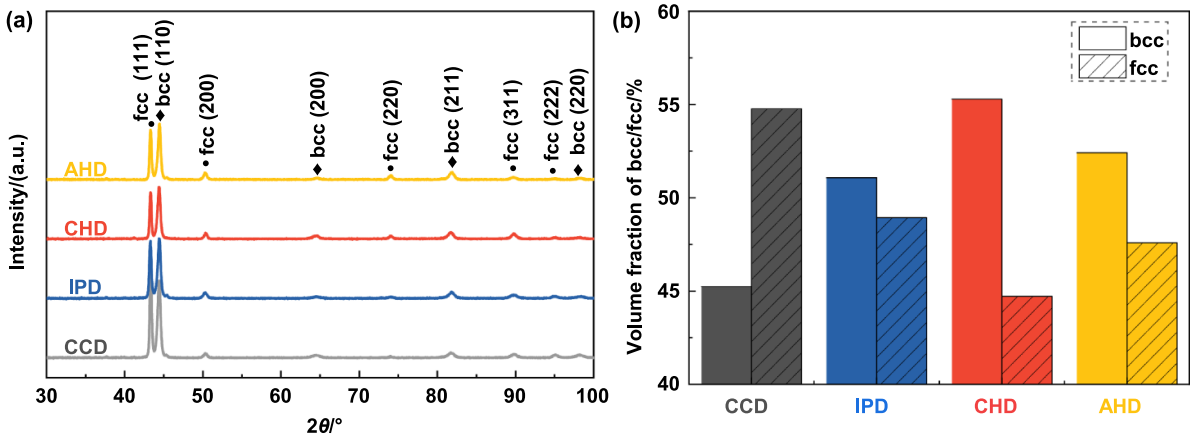

Figure 6. XRD patterns and phase analysis of the LDED-built Fe–Ni–Ti–Al steels printed under various thermal histories. (a) XRD patterns, (b) volume fraction of bcc and fcc phases.

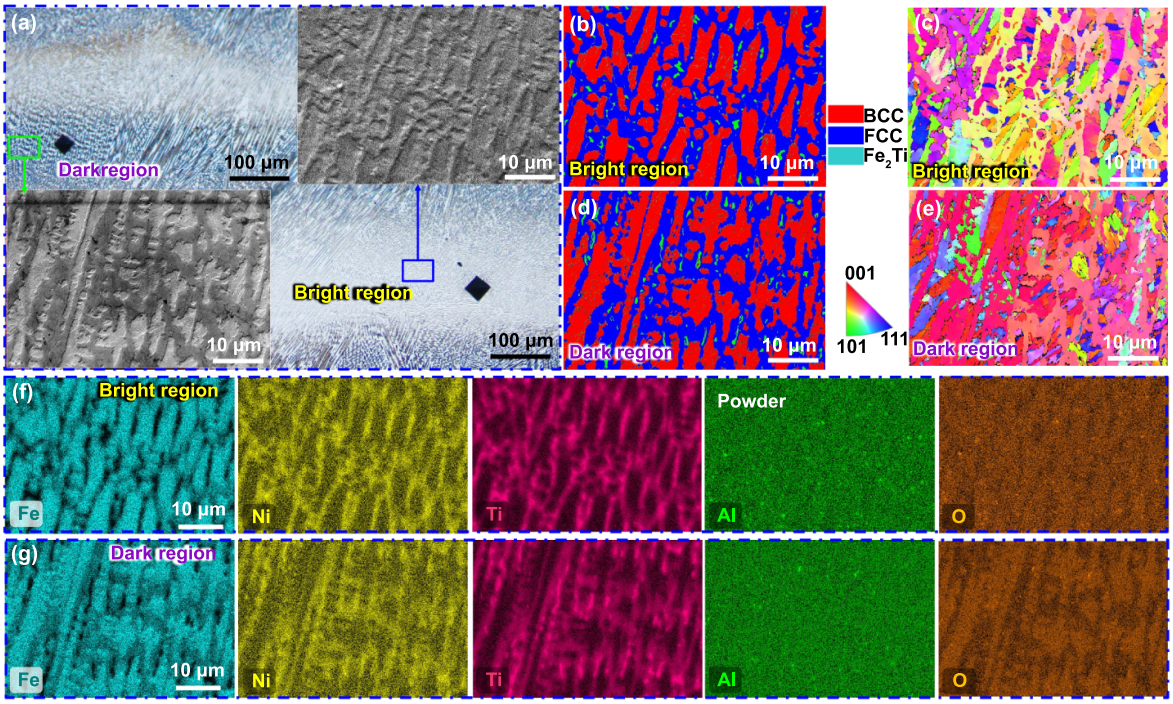

Figure 7. Microstructure of dark and bright regions of the IPD sample. (a) SEM and OM images of the IPD sample, (b) phase map and (c) IPF orientation maps of the bright region, (d) phase map and (e) IPF orientation maps of the dark region, and EDX mappings of the (f) bright region and (g) dark region (EDX taken during EBSD scan with scanning time more than 3 h).

than that in the CCD sample. This can be attributed to the heat accumulation during continuous deposition, which increases the resistance to martensitic transformation, as shown in the recorded temperature curves in figures 3(e) and (f). Hence, the bcc martensite fraction in the CCD sample is lower than that in the IPD sample. However, CHD has the highest volume fraction of the bcc martensite (~55%) among the four samples. The related phase transformation will be investigated in the following sections. For AHD, the intermediate volume fraction of bcc and fcc phases in the AHD sample can be ascribed to the unique alternated heating/cooling strategy.

As indicated above, a unique layer band structure is observed in the IPD sample. Further studies on microstructural differences in the dark and bright regions of the IPD sample are presented in figure 7. Notably, the dark region has a sharp microstructure and a rough surface, which is related to the martensitic transformation, internal stresses, volume changes, and crystallographic rearrangements, resulting in visible bulges or raised regions on the surface of the steel. The rough surface could scatter the light away when observed using OM, leading to darker appearances in OM observations [6]. In contrast, the bright regions are relatively smooth, suggesting that the degree of martensitic transformation in these areas is comparatively lower. The formation mechanism of the unique layerwise microstructure is associated with different cooling rates since the layer boundaries have a higher cooling

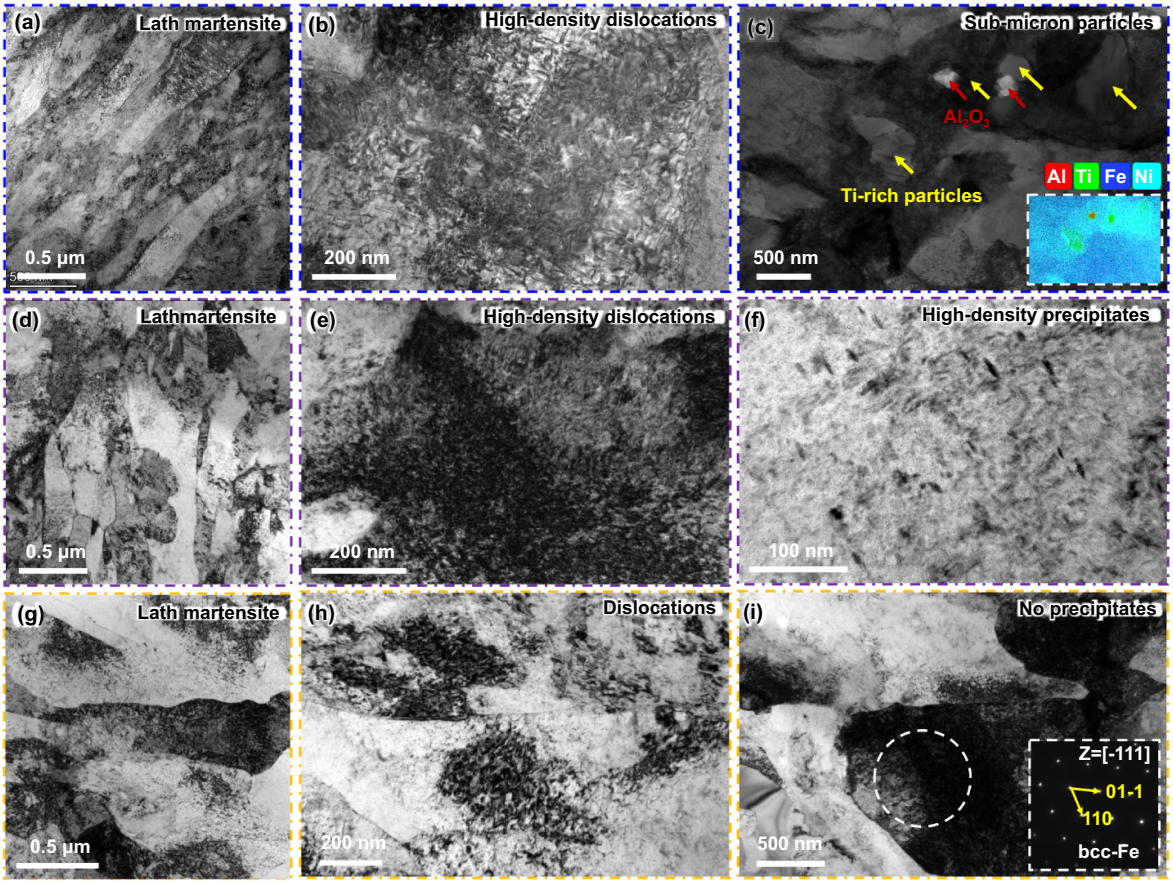

Figure 8. TEM analysis of the CCD and IPD samples. (a)–(c) CCD sample, (d)–(f) dark region and (g)–(i) bright region of the IPD sample.

rate and thermal gradient. Therefore, intensified martensitic transformation could occur in these regions. The EDX results in figures 7(f) and (g) show that the Ni and Ti elements both accumulate into the fcc phase. Besides, the dendritic arm space in the dark region (figure 7(g)) is also finer than that in the bright region (figure 7(f)), which further demonstrates that the cooling rate and thermal gradient in the dark region are higher than that in the bright region [26]. Additionally, the elemental mappings in figures 7(f) and (g) show that Al-rich particles correspond well with the O-rich particles, indicating that the Al_2O_3 particles are formed and the slight oxidation during printing.

3.2.3. Dislocations and secondary phases formation. Dislocations and multi-scale secondary phases in the LDED-built Fe–Ni–Ti–Al steel printed under various thermal histories are further characterised. For the CCD sample, lath martensite with high-density dislocations is the main microstructural feature, as shown in figures 8(a) and (b). The high-density dislocations are mainly from martensitic transformation and high residual stress levels in materials induced by rapid cooling [27]. Meanwhile, several Al_2O_3 particles are formed in the steel due to the oxidation (figure 8(c)). In addition, Ti has a strong segregation tendency during LDED, facilitating the formation of Ti-rich particles, as shown in figure 8(c). A similar phenomenon has also been reported in other Ti-containing maraging steels [6, 28]. In the IPD sample, lath morphology can be observed in both the dark and bright regions (figures 8(d) and (g)). However, the lath martensite in the dark regions is generally finer, and the dislocation density is higher compared to the bright regions. Besides, high-density rod-like nano-precipitates are formed in the dark regions (figure 8(f)), which can be inferred as *in-situ* formation during LDED deposition. However, no evident precipitate was found in the bright regions (figures 8(h) and (i)). The lower volume fraction of martensite along with a lower dislocation density reduced the driving force for *in-situ* precipitation. Because there are high-density dislocations in the Fe–Ni martensitic matrix, which could promote the heterogeneous nucleation at dislocations [6]. This microstructural difference of precipitates also explains why the hardness of the bright region is lower than that of the dark region, as shown in figure 4(g).

TEM analysis of the CHD sample is presented in figure 9. The lath martensite is observed in the CHD sample, as indicated in figure 9(a). Compared to the CCD and IPD samples in figure 8, the dislocation density of lath martensite in the CHD sample is relatively lower (figures 9(a) and (b)). Meanwhile, different types of sub-micron particles are found in the CHD sample (figure 9(b)). The SAED analysis on a particle along the [01–10] zone axis in figure 9(b) suggests that the large

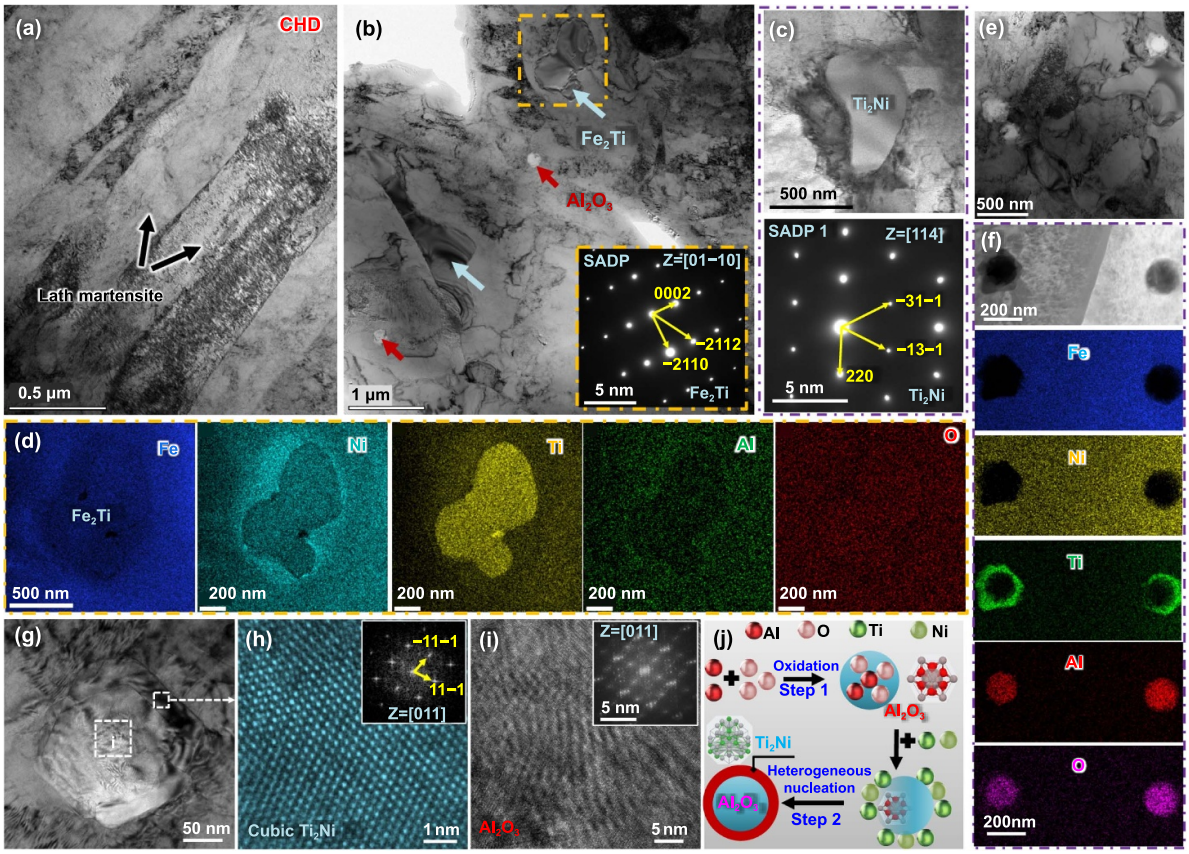

Figure 9. TEM analysis of the CHD sample. (a) Lath morphology, (b) Fe_2Ti and Al_2O_3 particles, (c) SAED analysis on a selected Ti_2Ni particle, (d) STEM-EDX mappings of a Fe_2Ti particle, (e) TEM observation and (f) STEM-EDX mapping analysis on the white spherical Al_2O_3 particles, (g) high-magnification view of a particle reveals a core–shell structure, (h) HRTEM observation on the shell region along with the FFT pattern deciphers the Ti_2Ni phase, (i) zoom-in image and corresponding FFT of the selected core region in image (g) reveals the Al_2O_3 phase, (j) schematic shows the formation mechanisms of the Al_2O_3 core and Ti_2Ni shell structure.

round-shape particles are the Fe_2Ti Laves phase, which can be further substantiated by the EDX mapping in figure 9(d) (corresponding to the inset in figure 9(b)). Figure 9(c) is the SAED along [114] zone axis of a pisiform particle, which indicates the Ti_2Ni Laves phase also forms in the CHD sample. In addition, 200–300 nm sized core–shell structured particles are found (figure 9(e)), rich in Ti, Al, and O elements (figure 9(f)). A closer observation of a particle in figure 9(g), together with EDX mapping in figure 9(f), reveals a core–shell structure where the core is rich in Al and O, and the shell is rich in Ti. The HRTEM and its corresponding fast Fourier transform (FFT) pattern shown in figure 9(h) indicate that the shell region is the bcc-Ti_2Ni phase. Likewise, the closer view and FFT of the centre region of the particle in figure 9(i) suggest the formation of the Al_2O_3 phase, indicating the oxidation of Al during printing at elevated temperatures. Notably, almost no η-Ni_3Ti precipitate is found in the CHD sample since the martensitic transformation is retarded during rapid solidification due to the fact that the substrate temperature is kept above Ms and the martensite in the CHD sample forms at a slow cooling rate containing fewer dislocations. For Fe–Ni–Ti maraging steels, the η-Ni_3Ti phase generally forms in the high dislocation density martensitic matrix, as it provides numerous nucleation sites for Ni_3Ti precipitates, and also due to its supersaturated nature (rich in Ni and Ti) [6, 20]. As such, although the higher temperature of CHD can promote the diffusion of alloying elements, there is hard to form η-Ni_3Ti precipitates *in situ* due to the lack of nucleation sites.

3.2.4. In-situ precipitation. As presented in figure 8(f), numerous precipitates are found in the dark bands of the IPD sample, which could contribute to the high hardness of these regions. A sample extract from the dark band via FIB was further analysed by TEM to characterise the precipitates, as shown in figure 10. Based on SAED, HAADF and EDX mapping analyses in figures 10(a)–(c), the precipitates are identified as the η-Ni_3Ti phase. The *in-situ* formation of η-Ni_3Ti precipitates could originate from the following aspects: (i) the martensitic transformation and thermal stress during cyclic thermal input in LDED produced high-density dislocations; (ii) the dislocation lines serve as easy pathways for promoting the diffusion of Ni, Ti, and Al elements and provide preferred sites for nucleation [29]; (iii) the subsequent cyclic thermal input of LDED serves as an *in-situ* aging treatment [7, 14], promoting the diffusion of Ni and Ti and *in-situ* precipitation of massive nano-sized η-Ni_3Ti eventually.

To quantitatively investigate the composition of the precipitates, the APT analysis on the dark bands of the IPD sample

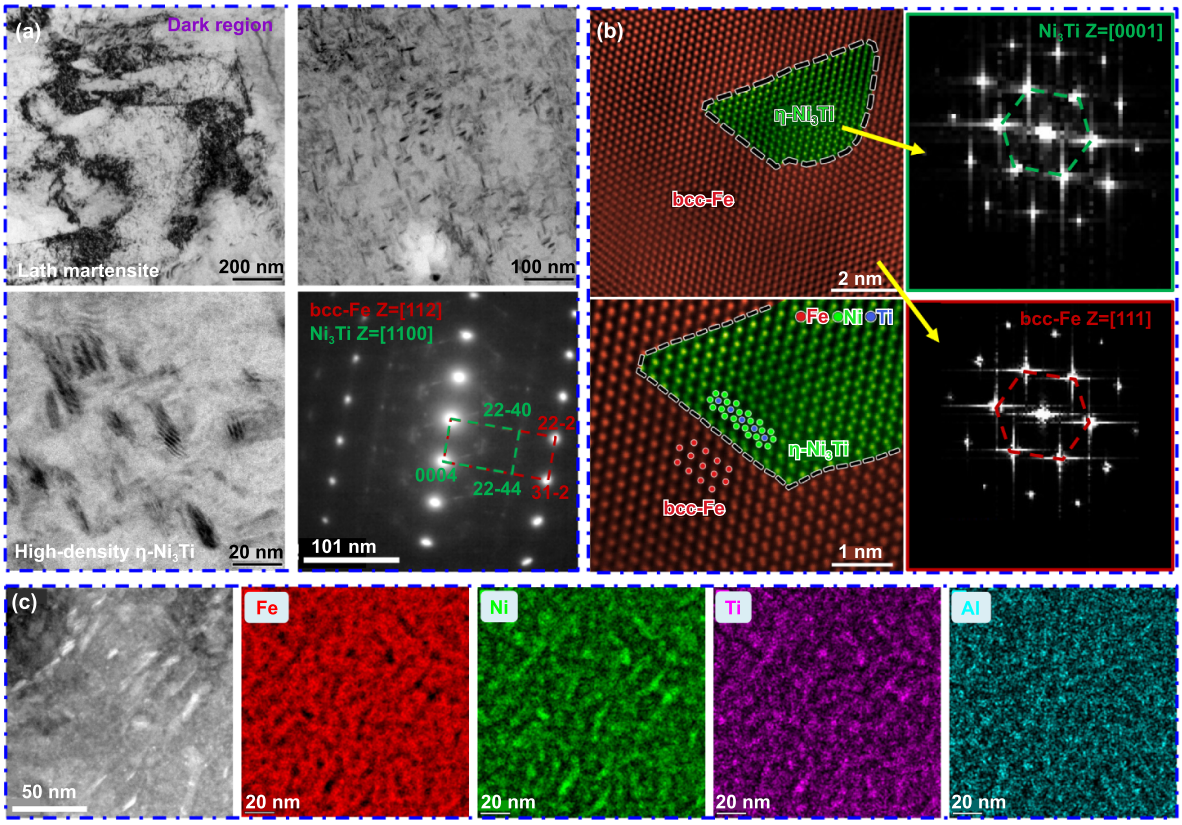

Figure 10. TEM analysis of precipitates in the dark regions of the IPD sample. (a) TEM images of the lath martensite, (b) high-resolution HADDF STEM images and FFTs of bcc-Fe and precipitates, and (c) STEM-EDX mappings of the η-Ni_3Ti precipitates.

is carried out (compared with bright regions) and presented in figure 11. Surprisingly, Al has also been involved in the *in-situ* precipitation process. The Ni, Ti, and Al-rich particles are observable in atom distribution maps in the dark band (figure 11(a)) but not found in the bright regions (figure 11(c)). The composition profile across a precipitate (figure 11(b)) indicates an atomic ratio of $Ni_{36}Ti_{14}Al_8$ among Ni, Ti, and Al. This suggests that the Al atom has substituted part of the Ti atom in η-Ni_3Ti and formed η-Ni_3(Ti, Al) solid solution, which has also been observed in Fe–Cr–Ni–Al–Ti maraging steels [30, 31]. Considering that the diffusion coefficient of Al in bcc-Fe is lower than that of Ni and Ti under the same temperature (figure 11(d)), it can be inferred that the η-Ni_3Ti formed in the primary stage, and Al then substitutes part of Ti in the η-Ni_3Ti phase to form the η-Ni_3(Ti, Al) solid solution.

3.3. Mechanical properties evaluation

Tensile tests were carried out to evaluate the mechanical properties of the LDED-built Fe–Ni–Ti–Al steels printed under various thermal histories. The tensile results are summarised in figure 12 and table 2, respectively. Interestingly, as depicted in figure 12(a), the LDED-built Fe–Ni–Ti–Al steels under different thermal histories exhibit a large range of mechanical properties with tensile strengths expanding from 1.24 to 1.54 GPa and elongation ranging from 8.1% to 19.3%. Heating the substrate improves the ductility significantly, despite a moderate decrease in tensile strength. Among the four samples, the IPD sample has the highest ultimate tensile strength (UTS) of 1.54 GPa with a moderate elongation of ~8.1%, while the CHD sample owns the highest elongation of 19.3% with a reduced UTS of 1.24 GPa. The work-hardening capacity (defined as UTS minus yield strength) of the IPD sample reaches 572 MPa, indicating the highest work-hardening capacity. The CHD sample, according to the strain-hardening rate curves in figure 12(b), exhibits a significantly longer work-hardening plateau compared to the CCD and IPD samples, indicating a more stable work-hardening behaviour. The AHD sample fractured prematurely (elongation 3.7%), which could be caused by oxidation during the prolonged interlayer heating/cooling process. Consequently, subsequent studies on deformation and fracture behaviour, as well as strengthening mechanisms, will mainly focus on the CCD, IPD, and CHD samples.

4. Discussion

4.1. Mechanisms of phase transformation and multi-scale phases formation

For the studied Fe–Ni–Ti–Al steel, the phase transformation behaviour and elemental segregation dominate the microstructural formation. To further understand the effect of

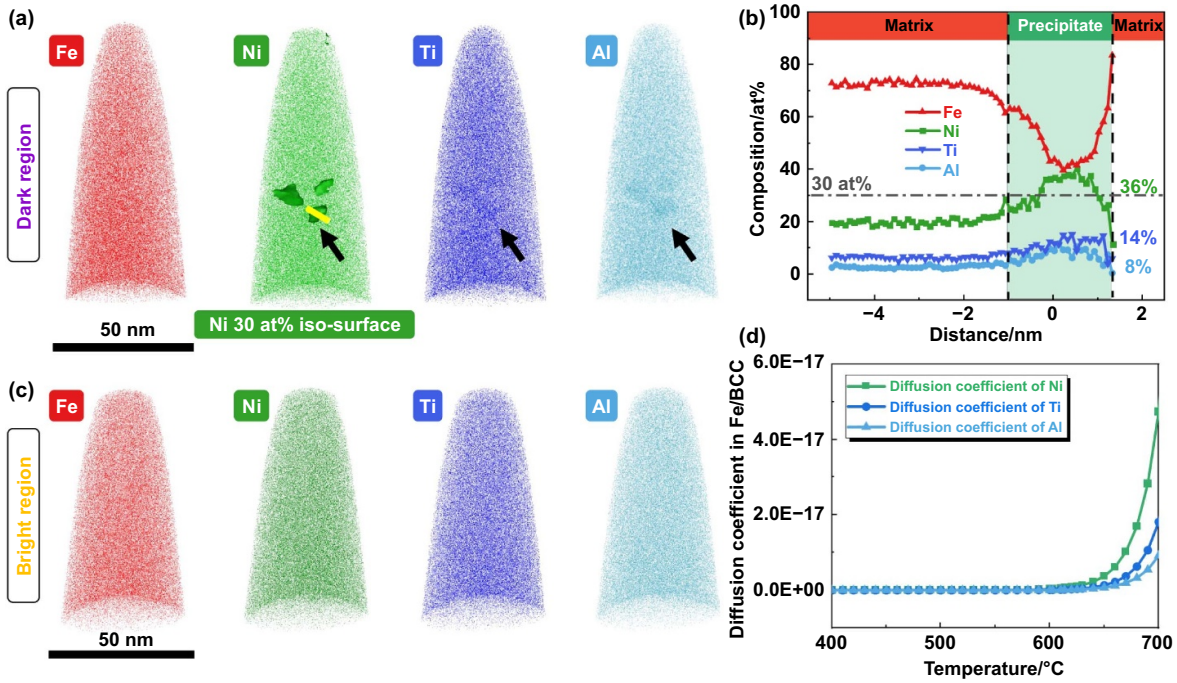

Figure 11. APT analysis of the dark and bright regions of the IPD sample. (a) Atom distribution maps of the dark regions, (b) composition profile across a precipitate along the yellow rectangle, (c) atom maps of the bright regions, (d) diffusion coefficients of Ni, Ti, and Al in the bcc-Fe calculated by Thermo-Calc.

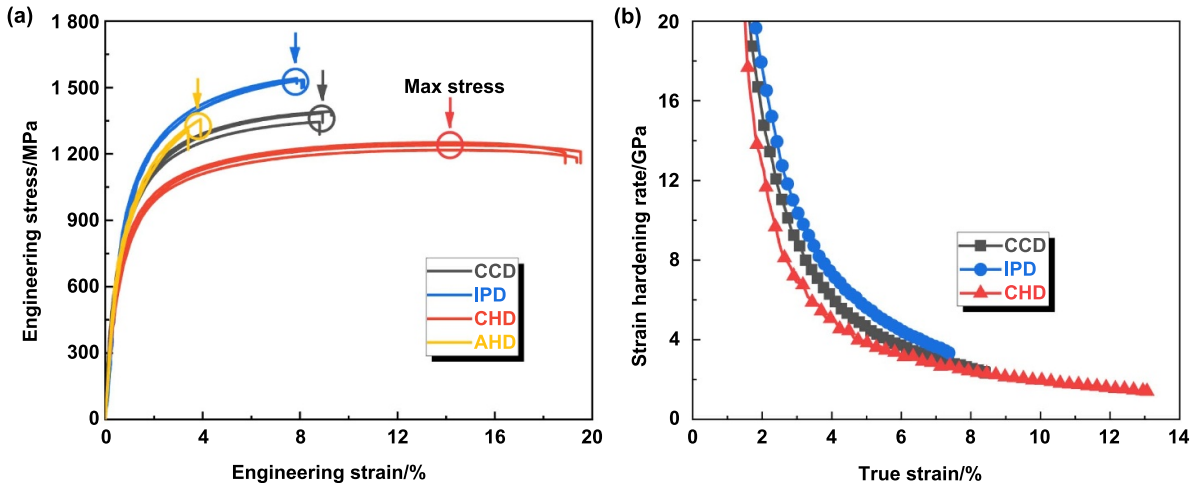

Figure 12. Tensile results of the LDED-built Fe–Ni–Ti–Al steels under various thermal histories. (a) Tensile engineering stress-strain curves and (b) strain hardening rate curves.

Table 2. Tensile properties of the LDED-built Fe–Ni–Ti–Al steels printed under various thermal histories.

Sample	Yield strength (MPa)	Ultimate tensile strength (MPa)	Work hardening capacity (MPa)	Uniform elongation (%)	Elongation at fracture (%)
CCD	824 ± 15	1365 ± 31	541	9.0 ± 0.3	9.0 ± 0.3
IPD	966 ± 22	1538 ± 5	572	8.1 ± 0.2	8.1 ± 0.2
CHD	747 ± 9	1236 ± 14	489	13.8 ± 0.3	19.3 ± 0.3
AHD	837 ± 7	1331 ± 25	494	3.7 ± 0.3	3.7 ± 0.3

elemental segregation on phase formation of the steel printed under various thermal histories, the CALPHAD analysis is carried out for the Fe–Ni–Ti–Al steel, and the results are shown in figure 13. Under the equilibrium condition, the one-axis phase diagram indicates that Laves phase (i.e. Fe_2Ti and Ti_2Ni) and η-Ni_3Ti would form after cooling down, which

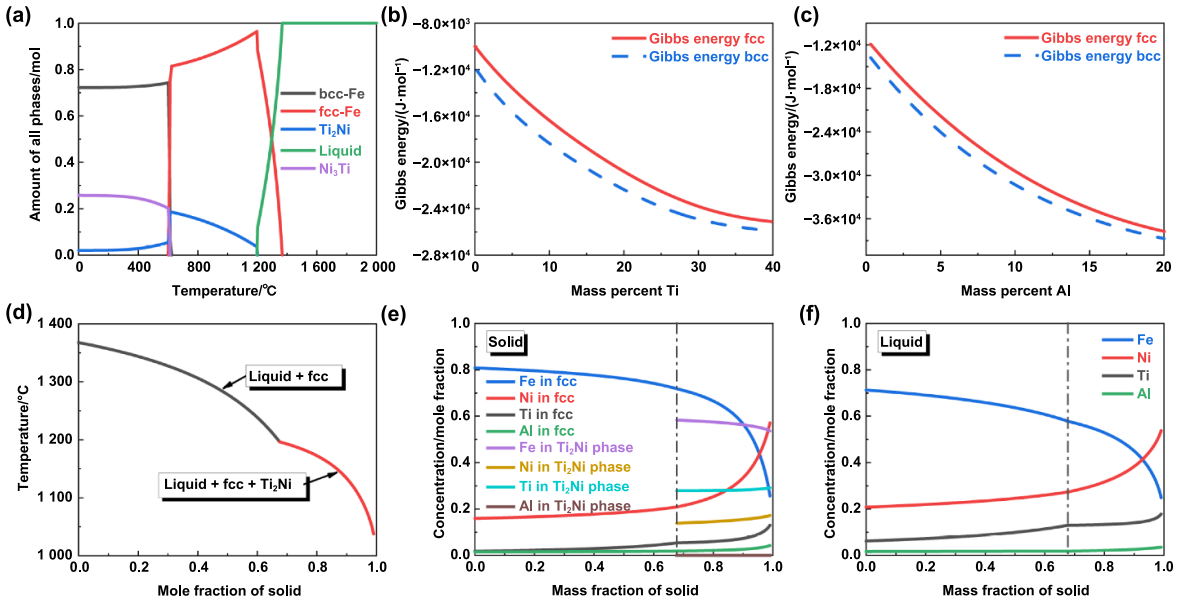

Figure 13. Thermodynamic calculation of the Fe–Ni–Ti–Al steel. (a) One-axis equilibrium phase diagram, the Gibbs free energies of single-phase bcc and fcc (b) for varying Ti content (maintaining a fixed Ni content of 20.8 wt% and a fixed Al content of 1.7 wt%), (c) for varying Al content (maintaining a fixed Ni content of 20.8 wt% and a fixed Ti content of 6.2 wt%), (d) the Scheil solidification curve of the Fe–Ni–Ti–Al steel, (e) and (f) the concentrations of elements in solid and liquid phases as a function of the mass fraction of solid.

has been verified by the TEM and EBSD results. Besides, the Gibbs free energies of single-phase bcc and fcc for a variable Ti content and Al content are calculated and displayed in figure 13(b). Notably, the Gibbs energy difference between the fcc and bcc phases decreases with increasing Ti content, indicating that the Ti acts as an fcc austenite stabiliser in the studied steel. As a result, it is understandable that the Ti element is accumulated at the fcc phase regions (figure 7). For the Al element, there is no apparent segregation as it has a margin influence on the Gibbs energy difference between the fcc and bcc phases in this steel. Given the typical non-equilibrium nature of the LDED process, the classical Scheil model is employed to evaluate the elemental segregation behaviour of the Fe–Ni–Ti–Al steel during rapid solidification [29]. The Scheil curve in figure 13(d) reveals that the fcc and Laves phases formed during the rapid solidification process. The evolutions of the elemental concentration in solid and liquid during non-equilibrium solidification are presented in figures 13(e) and (f), respectively. During the rapid solidification process, the segregation of Ti tends to stabilise the fcc phase gradually. In the final stage of solidification, local segregation of the Ti element promotes the formation of Laves phases (i.e. Fe_2Ti and Ti_2Ni). This is consistent with the observations made in the TEM analysis presented in figure 9.

For the different deposition strategies, the different thermal histories experienced affect the element segregation and phase formation. During CCD, the gradually increasing substrate temperature affected the dislocation density and secondary phase formation in the initial layers. Nevertheless, the substrate temperature will become stable with the increasing deposition layer number during CCD, and the thermal accumulation (figure 3(a)) could partially retard martensitic transformation. As a result, no dark bands and *in-situ* η-Ni_3Ti precipitations are found within the CCD sample. In contrast, the interlayer paused strategy mitigated the thermal accumulation in the IPD sample (figure 3(b)), facilitating the martensitic transformation in the whole building. Meanwhile, the formation of parallel bcc-rich dark bands could be related to the high cooling rate at the layer interface. Further thermal cycling of IPD promotes the *in-situ* precipitation of η-Ni_3Ti, leading to higher hardness in these bands, as exhibited in the hardness results in figure 4(g).

Notably, the CHD sample exhibits a lower fraction of austenite and a higher fraction of martensite compared to the IPD and CCD samples, which is associated with the elements' diffusion and segregation. Generally, the formation of austenite in maraging steel during LDED is associated with the micro-segregation of austenite stabilisers that occurs during rapid solidification [32]. For IPD and CCD, the rapid cooling rate led to the micro-segregation of alloying elements during solidification (shown in figure 7), which promoted the formation of austenite at room temperature, with evidence showing Ni and Ti elements accumulation in the fcc phase. In contrast, substrate heating in CHD promoted elemental diffusions and reduced element segregation (e.g. Ni and Ti) during deposition, reducing austenite formation. Moreover, the formation of the Fe_2Ti and Ti_2Ni Laves phases in the CHD sample during printing depletes part of austenite stabiliser (i.e. Ni and Ti), which reduces the stability of austenite and further promotes the martensite formation. Nevertheless, it can be inferred that the dislocation density in the martensite of the CHD sample are lower than that in the CCD and IPD samples due to the lower cooling rate. This is the main reason that the strength of the CHD sample is the lowest among the samples despite the highest volume fraction of bcc martensite.

The formation of sub-micron Al_2O_3 particles also plays a vital role in the mechanical performance of the LDED-built steels. The oxidation of Fe, Ni, Ti, and Al elements in the steel makes it possible to form FeO, NiO, TiO_2, and Al_2O_3 in the Fe–Ni–Ti–Al steel, respectively. However, among the four constitutive elements, Al has the lowest equilibrium partial pressures of oxygen [33]; thus, from thermodynamic consideration, Al_2O_3 is the most likely oxide to form in this material, owing to its lowest Gibbs energy [33]. This also indicates that the Al element can deplete oxygen during LDED, thereby mitigating the adverse effects of oxidation under substrate heating deposition. Moreover, it is worth noting that the Al_2O_3 particles could act as the nuclei site for Ti segregation, as depicted in figure 9(j). Similar phenomena are also reported in AM-processed Ni-based superalloys, where Al_2O_3 acts as the nucleation site for the formation of inclusions during solidification [34, 35]. The formation of Ti-rich layers on the Al_2O_3 particles could enhance the interfacial bonding between the Al_2O_3 particles and the matrix, thereby ensuring the high mechanical properties of the steel.

4.2. Strengthening and toughening mechanisms

As shown in figure 14(a), compared with most AM-built commercial materials, the LDED-built Fe–Ni–Ti–Al steels achieve superior mechanical performance via tailoring thermal history without the adjustment of energy-related process parameters. Notably, the IPD sample has the highest tensile strength (~1.54 GPa) among the four studied samples, which is ~302 MPa higher than that of the CHD sample (~1.24 GPa), indicating a large range tunable mechanical strength. Herein, the strengthening mechanisms of the IPD sample are estimated and compared with the CHD sample to reveal the underlying reason for such a large strength difference. Considering that the 5–50 nm sized η-Ni_3(Ti, Al) precipitates are enough to resist the movement of dislocations, the strengthening contribution of the precipitates can be calculated according to the Orowan bowing mechanism [22]:

$$\sigma_0 = \frac{Gb}{2\pi K(\lambda - d)} \ln\left(\frac{\lambda - d}{2b}\right) \tag{3}$$

$$\frac{1}{K} = \frac{1}{2}\left(\frac{1}{1-\nu} + 1\right) \tag{4}$$

where G is the shear modulus of the matrix (64 GPa) [36], b is the Burgers vector (0.249 nm) [22], λ is the interspace of the precipitates (~15 nm), ν is the Poisson's ratio of the matrix, and K is a parameter related to ν ($K = 0.82$, $\nu = 3$), d is the average diameter of the precipitates. The average diameter and length of the η-Ni_3(Ti, Al) precipitates are about 4 nm and 17 nm, respectively. The equivalent diameter d of the η-Ni_3(Ti, Al) precipitates is simplified as 7.5 nm. According to equations (3) and (4), the strengthening contribution of η-Ni_3(Ti, Al) precipitates is calculated as 1118 MPa. However, the η-Ni_3(Ti, Al) precipitates are exclusively formed in the dark bands, which account for approximately 38% of the entire IPD sample; hence, the precipitation strengthening of

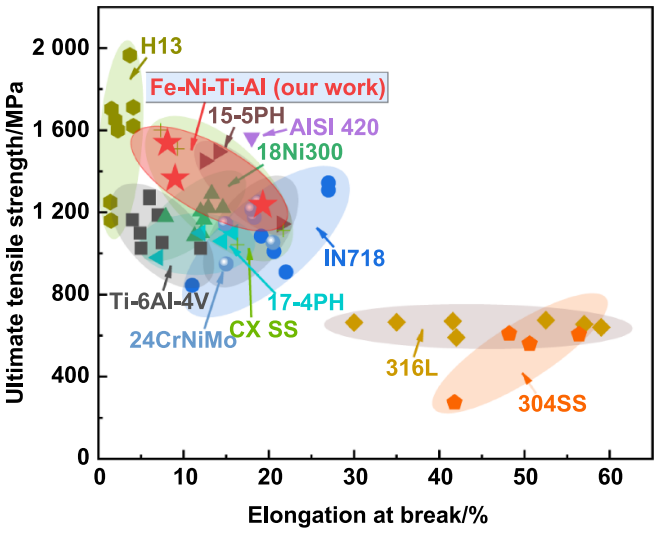

Figure 14. Ashby plot of tensile properties of the LDED-built Fe–Ni–Ti–Al maraging steels compared with AM-built high-strength commercial materials (all the data points are in as-built state), including maraging steels (e.g. 18Ni300) [38], precipitation hardening stainless steels (e.g. 17–4PH, 15–5PH and CX SS) [38], tool steels (e.g. H13) [38], martensitic stainless steels (e.g. AISI 420) [39], high-strength low-alloy steels (e.g. 24CrNiMo) [38], Ti alloys (e.g. Ti–6Al–4V) [40], Ni-based alloys (e.g. IN718) [40].

η-Ni_3(Ti, Al) to the IPD sample is ~425 MPa. For the CHD sample, the high substrate temperature reduces the degree of supersaturated solid solubility of Ni and Ti and the dislocation density within the martensite, resulting in no precipitate formation during printing. Besides, based on the TEM observations, the average thickness of lath martensite of the IPD and CHD samples are determined to be 0.273 and 0.356 nm, respectively. According to the Hall–Petch equation, the grain boundary strengthening can be estimated by:

$$\sigma_{GB} = kD^{-1/2} \tag{5}$$

where the Hall–Petch coefficient is estimated as 149 MPa·$\mu m^{-1/2}$ based on the previous [37]. The difference in grain boundary strengthening between the IPD and the CHD samples is determined to be ~35 MPa. According to the tensile results, the UTS of the IPD sample is ~302 MPa higher than that of the CHD sample. As a result, the primary contributor to strength improvements can be attributed to the *in-situ* precipitation of high-density η-Ni_3Ti. For the AHD sample, the yield strength and UTS are both located between the CHD and IPD samples, owing to the application of the alternative heating/cooling strategy.

The CHD sample possesses superior ductility (with an elongation of 19.3%), which surpasses most of the AM-built advanced high-strength steels. To reveal the underlying deformation mechanisms, the EBSD analysis is further conducted on the CHD samples before and after tensile tests, as shown in figure 15. The Fe_2Ti Laves phase undergoes significant strain during the tensile tests, changing from its original particle shape to a long strip shape. The Fe_2Ti Laves

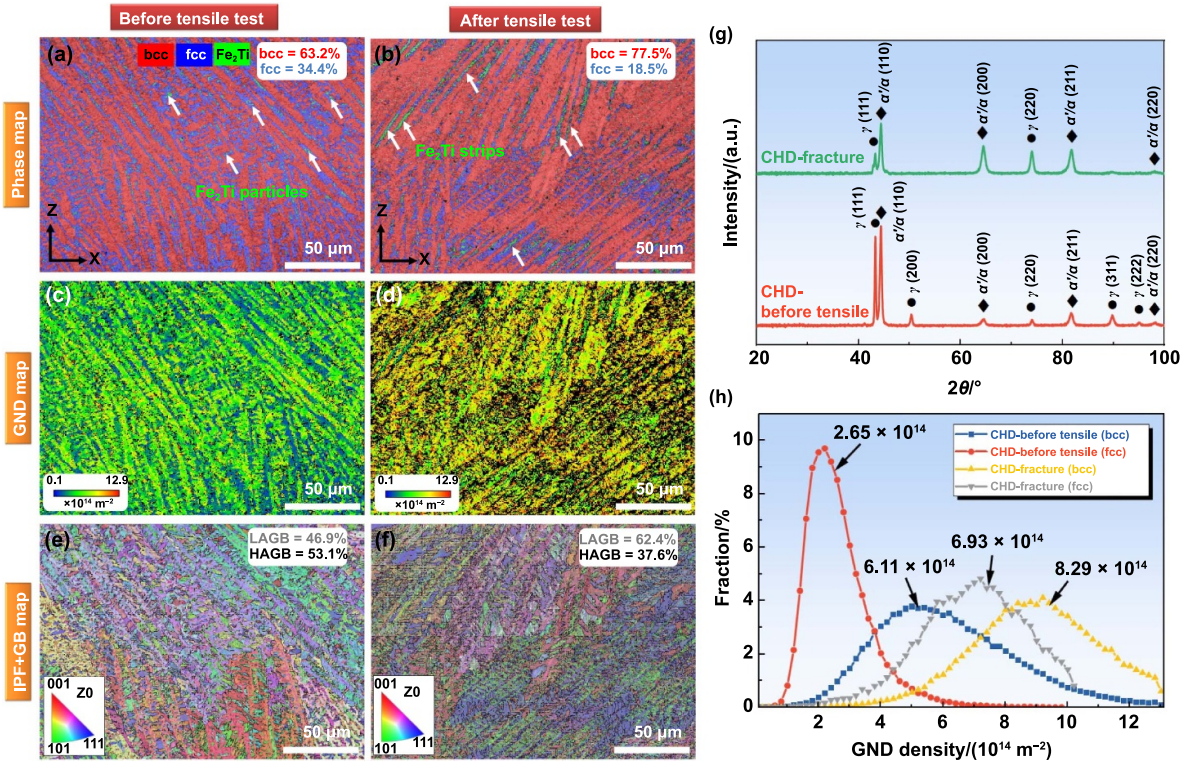

Figure 15. EBSD and XRD analysis of the CHD sample before and after tensile tests. (a) and (b) EBSD phase maps, (c) and (d) GND maps, (e) and (f) IPF + GB maps, (g) XRD patterns, (h) GND density of the bcc and fcc phases.

phase is generally considered harmful to the ductility and work-hardening capacity of steel [41]. However, in the CHD sample, the Fe_2Ti Laves phases are wrapped inside the soft fcc phase during tensile deformation, and thus, the Fe_2Ti Laves phase is considered not harmful to the ductility. More importantly, the fraction of the fcc phase reduces from 34.4% to 18.5% while the bcc phase increases from 63.2% to 77.5% after the tensile test, indicating transformation-induced plasticity (TRIP) phenomenon (figures 15(a) and (b)), i.e. The TRIP effect significantly contributed to the superior work-hardening capacity of the steel [42]. The TRIP phenomenon can also be demonstrated by the XRD patterns in figure 15(g), in which the intensity of bcc peaks increased significantly after the tensile test (i.e. fcc $\rightarrow$ bcc phase transformation). Meanwhile, the residual stress between the bcc and fcc phases in the CHD sample is released due to the high substrate temperature and the lowered cooling rate. The equilibrium fcc + bcc dual-phase microstructure could also contribute to the superior work-hardening capacity of the steel. Compared with the bcc martensite, the GND density of the fcc austenite in the CHD sample increased significantly after the tensile test (from 2.65 $\times$ 10^{14} m^{-2} to 6.93 $\times$ 10^{14} m^{-2}), as shown in figure 15(h). Meanwhile, the fraction of low-angle grain boundary (2°–10°) increased from 46.9% to 62.4% (figures 15(e) and (f)), indicating that the fcc phase accommodate significant plastic strain during deformation.

For the CCD and IPD samples, the moderate uniform elongation can be mainly attributed to the fcc/bcc dual-phase microstructure, in which the fcc phase can accommodate plastic strain in the initial stage. For the IPD sample, the hetero-deformation between the dark and bright regions could also improve the work-hardening capacity of the steel [43]. Besides, the high-density dislocations and *in-situ* formed precipitates in the IPD and CCD samples will lead to stress concentration during the tensile test, which thereby leads to a lower uniform elongation than the CHD sample.

4.3. Mechanisms for large tunable mechanical properties

Overall, the tensile test results reveal that a wide range of mechanical properties can be achieved by tailoring the thermal history. Unlike most previous studies, which primarily tailor properties by post heat treatments or adjusting energy-related process parameters (e.g. laser power, scan speed, and hatch spacing), the current work aims to tailor properties by adjusting the thermal history without changing these process parameters. The underlying mechanism for the large-range tunable mechanical property is mainly associated with the unique tunable thermal history of LDED and the high microstructure sensitivity of the Fe–Ni–Ti–Al maraging steel to thermal history. The thermal gradient and cooling rate play a significant role in controlling the phase transformation behaviour, hereby affecting the dislocation density and bcc/fcc phase fraction. Besides, the intrinsic thermal cycling of LDED can induce an *in-situ* aging treatment to the solidified material, producing high-density precipitates to strengthen the material effectively.

The schematic diagrams of microstructural formation mechanisms of the steel printed with thermal history control

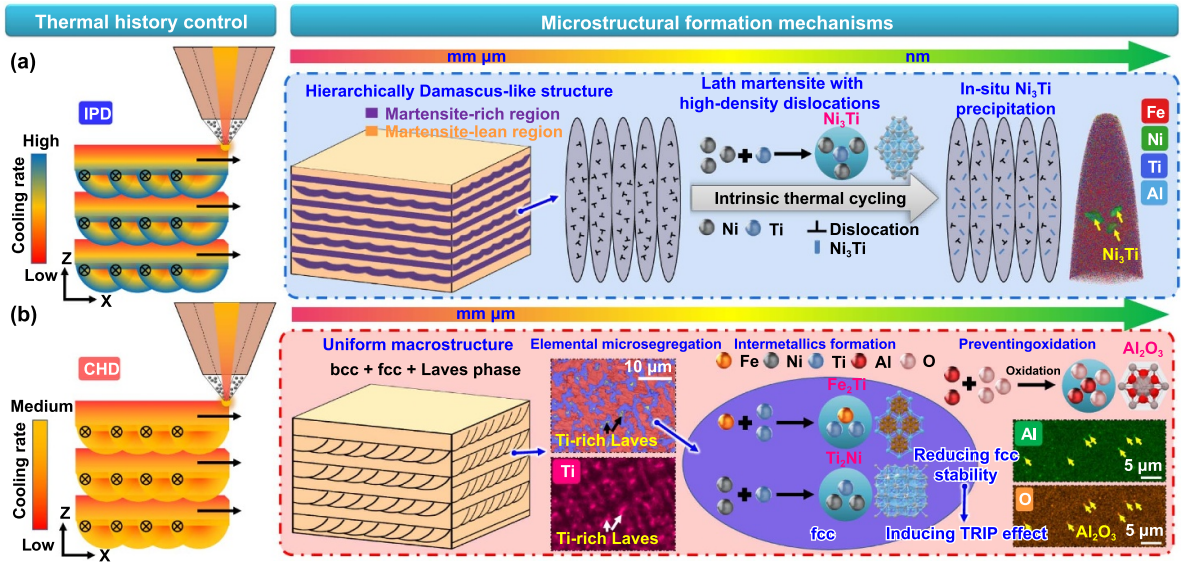

Figure 16. Schematic diagrams of microstructural formation mechanisms with thermal history control. (a) IPD and (b) CHD.

are illustrated in figure 16. For the IPD sample, the high tensile strength mainly originates from: (i) high-density dislocations in the martensitic matrix due to intensified cooling rate by interlayer pause deposition approach; (ii) plenty of η-Ni_3(Ti, Al) precipitates formed due to the intrinsic heat treatment of LDED (figure 16(a)). In contrast, in the CHD sample, dislocation density in the matrix is much lower than IPD due to the reduced temperature gradient by substrate heating, which could inhibit *in-situ* precipitation via heterogeneous nucleation on dislocations. Besides, there is no evident η-Ni_3(Ti, Al) precipitate observed in the CHD sample. Consequently, the CHD sample obtained a lower tensile strength (1.24 GPa) than the IPD sample (1.54 GPa).

The ductility also heavily depends on the thermal history experienced, as different microstructure characteristics can significantly affect the material's deformation behaviour. In the IPD sample, the hetero-deformation between the hard dark bands and the soft bright regions is considered to enhance the work-hardening capacity of the steel via strain partitioning and back stress formation [43]. However, stress concentration occurs at the interface between the dark bands and the bright regions during tensile deformation due to strain mismatch. Consequently, no necking stage is observed in the tensile curves of the IPD sample (figure 12(a)). In contrast, the CHD sample exhibits a long necking stage and a much larger break elongation, representing a better damage tolerance. The main reason can be attributed to its uniform microstructure, which leads to a more uniform strain distribution. Meanwhile, the formation of Fe_2Ti and Ti_2Ni Laves phase inside the fcc austenite depletes part of Ni and Ti, thereby reducing the phase stability of fcc austenite and inducing the TRIP effect more effectively (figure 16(b)). The soft fcc austenite phase can accommodate significant strain (figure 15(h)), and the dislocations generated within the fcc phase could provide significant driving force for the occurrence of TRIP. Moreover, the Al element captures oxygen and forms micro-sized Al_2O_3 particles during printing, mitigating the negative impact of oxidation on the ductility of the steel. This aspect is particularly critical for the CHD sample, as CHD is conducted at a high substrate temperature, making it more susceptible to oxidation. Last but not least, the reduced dislocation density and residual stress relaxation are also favourable for achieving better damage tolerance in the CHD sample. Overall, the tunable ductility of the steel can be attributed to the combined effects of these microstructural formation mechanisms.

5. Conclusions

In this work, a novel Fe–Ni–Ti–Al maraging steel with rapid precipitation kinetics was processed by LDED using different deposition strategies, including continuous, interlayer paused, constant heating, and alternative heating deposition. Different thermal histories were experienced during the LDED of Fe–Ni–Ti–Al to achieve different microstructures and large ranges of tunable mechanical properties. The main conclusions are:

(1) The microstructural evolution of the Fe–Ni–Ti–Al steel is sensitive to the thermal history during LDED. Versatile mechanical properties of the steel are obtained via tailoring thermal history. The IPD strategy has proven advantageous in achieving high strength (~1.54 GPa) with moderate ductility (~with an E_f of 8.1%). In contrast, the CHD strategy can attain superior ductility (~with an E_f of 19.3%) with moderate strength (~1.24 GPa). The achievable mechanical property range via tailoring thermal history in the LDED-built Fe–Ni–Ti–Al steel is significantly larger than most commercial materials.

(2) The tunable strength of the LDED-processed Fe–Ni–Ti–Al steel is mainly associated with the dislocations in the martensitic matrix due to different cooling rates by different deposition strategies, and the *in-situ* formation

of η-Ni_3(Ti, Al) precipitates due to the intrinsic heat treatment of the LDED process.

(3) The tunable ductility of LDED-processed Fe–Ni–Ti–Al steel can be attributed to (i) the Ti-rich Laves phase (i.e. Fe_2Ti and Ti_2Ni) depleted Ti and Ni elements in the fcc phase, thereby reducing the fcc phase stability and inducing the TRIP effect during deformation, (ii) the formation of Al_2O_3 particles as a result of the strong affinity between Al and O protected the steel from oxidation, (iii) the reduced dislocation density and residual stress relaxation benefit a superior work-hardening capacity.

These findings emphasize the pivotal role of thermal history in shaping the microstructure and programming strength-ductility combinations of AM-processed materials. The materials innovation alongside strategic thermal history control emerges as an effective approach for developing high-performance metallic materials with wide and programmable strength-ductility combinations tailored for different service circumstances.

Acknowledgment

This work was financially supported by the Career Development Fund (Grant No. C210112051) under the Agency for Science, Technology and Research (A*STAR) of Singapore and 2022 MTC Young Individual Research Grants (Grant No: M22K3c0097) under Singapore Research, Innovation and Enterprise (RIE) 2025 Plan, led by C Tan.

ORCID iDs

Jinlong Su https://orcid.org/0000-0002-2120-1835
Chaolin Tan https://orcid.org/0000-0003-2029-4600

References

[1] Su J L *et al* 2024 Recent innovations in laser additive manufacturing of titanium alloys *Int. J. Extrem. Manuf.* **6** 032001
[2] Tan C L, Deng C, Li S, Abena A, Jamshidi P, Essa K, Wu L K, Xu G H, Attallah M M and Liu J 2022 Mechanical property and biological behaviour of additive manufactured TiNi functionally graded lattice structure *Int. J. Extrem. Manuf.* **4** 045003
[3] Bouabbou A and Vaudreuil S 2022 Understanding laser-metal interaction in selective laser melting additive manufacturing through numerical modelling and simulation: a review *Virtual Phys. Prototyp.* **17** 543–62
[4] Tan C L, Weng F, Sui S, Chew Y and Bi G J 2021 Progress and perspectives in laser additive manufacturing of key aeroengine materials *Int. J. Mach. Tools Manuf.* **170** 103804
[5] Liu T S, Chen P, Qiu F, Yang H Y, Jin N T Y, Chew Y, Wang D, Li R D, Jiang Q C and Tan C L 2024 Review on laser directed energy deposited aluminum alloys *Int. J. Extrem. Manuf.* **6** 022004
[6] Kürnsteiner P, Wilms M B, Weisheit A, Gault B, Jägle E A and Raabe D 2020 High-strength Damascus steel by additive manufacturing *Nature* **582** 515–9
[7] Kürnsteiner P, Wilms M B, Weisheit A, Barriobero-Vila P, Jägle E A and Raabe D 2017 Massive nanoprecipitation in an Fe-19Ni-*x*Al maraging steel triggered by the intrinsic heat treatment during laser metal deposition *Acta Mater.* **129** 52–60
[8] Su J L, Jiang F L, Tan C L, Weng F, Ng F L, Goh M H, Xie H M, Liu J, Chew Y and Teng J 2023 Additive manufacturing of fine-grained high-strength titanium alloy via multi-eutectoid elements alloying *Composites* B **249** 110399
[9] Herzog D, Seyda V, Wycisk E and Emmelmann C 2016 Additive manufacturing of metals *Acta Mater.* **117** 371–92
[10] Li H K, Thomas S and Hutchinson C 2022 Delivering microstructural complexity to additively manufactured metals through controlled mesoscale chemical heterogeneity *Acta Mater.* **226** 117637
[11] Huang S, Narayan R L, Tan J H K, Sing S L and Yeong W Y 2021 Resolving the porosity-unmelted inclusion dilemma during *in-situ* alloying of Ti34Nb via laser powder bed fusion *Acta Mater.* **204** 116522
[12] Zhang J Q, Bermingham M, Otte J, Liu Y G and Dargusch M 2023 Towards uniform and enhanced tensile ductility of additively manufactured Ti-5Al-5Mo-5V-3Cr alloy through designing gradient interlayer deposition time *Scr. Mater.* **223** 115066
[13] Xu W, Lui E W, Pateras A, Qian M and Brandt M 2017 *In situ* tailoring microstructure in additively manufactured Ti-6Al-4V for superior mechanical performance *Acta Mater.* **125** 390–400
[14] Kürnsteiner P, Barriobero-Vila P, Bajaj P, De Geuser F, Wilms M B, Jägle E A and Raabe D 2023 Designing an Fe-Ni-Ti maraging steel tailor-made for laser additive manufacturing *Addit. Manuf.* **73** 103647
[15] Tan C L *et al* 2023 Review on field assisted metal additive manufacturing *Int. J. Mach. Tools Manuf.* **189** 104032
[16] Mertens R, Dadbakhsh S, Van Humbeeck J and Kruth J P 2018 Application of base plate preheating during selective laser melting *Proc. CIRP* **74** 5–11
[17] Kempen K, Vrancken B, Buls S, Thijs L, Van Humbeeck J and Kruth J P 2014 Selective laser melting of crack-free high density M2 high speed steel parts by baseplate preheating *J. Manuf. Sci. Eng.* **136** 061026
[18] Ding C G, Cui X, Jiao J Q and Zhu P 2018 Effects of substrate preheating temperatures on the microstructure, properties, and residual stress of 12CrNi2 prepared by laser cladding deposition technique *Materials* **11** 2401
[19] Su J L, Ji X K, Liu J, Teng J, Jiang F L, Fu D F and Zhang H 2022 Revealing the decomposition mechanisms of dislocations and metastable α' phase and their effects on mechanical properties in a Ti-6Al-4V alloy *J. Mater. Sci. Technol.* **107** 136–48
[20] Cui C, Leitner H, Platl J and Schnitzer R 2023 Influence of platform preheating on *in situ* precipitation in an FeCoMo alloy during laser powder bed fusion *Mater. Charact.* **197** 112689
[21] Wei C, Zhang Z Z, Cheng D X, Sun Z, Zhu M H and Li L 2021 An overview of laser-based multiple metallic material additive manufacturing: from macro- to micro-scales *Int. J. Extrem. Manuf.* **3** 012003
[22] Tan C L, Zhou K S, Ma W Y, Zhang P P, Liu M and Kuang T C 2017 Microstructural evolution, nanoprecipitation behavior and mechanical properties of selective laser melted high-performance grade 300 maraging steel *Mater. Des.* **134** 23–34
[23] Tan C L *et al* 2023 Machine learning customized novel material for energy-efficient 4D printing *Adv. Sci.* **10** 2206607
[24] Tanaka M and Choi C S 1972 The effects of carbon contents and M_S temperatures on the hardness of martensitic Fe-Ni-C alloys *Trans. Iron Steel Inst. Japan* **12** 16–25

[25] Olson D L 1985 Prediction of austenitic weld metal microstructure and properties *Weld. J.* **64** 281S–95S
[26] DebRoy T, Wei H L, Zuback J S, Mukherjee T, Elmer J W, Milewski J O, Beese A M, Wilson-Heid A, De A and Zhang W 2018 Additive manufacturing of metallic components—process, structure and properties *Prog. Mater. Sci.* **92** 112–224
[27] Bertsch K M, Meric de Bellefon G, Kuehl B and Thoma D J 2020 Origin of dislocation structures in an additively manufactured austenitic stainless steel 316L *Acta Mater.* **199** 19–33
[28] Kwiatkowski da Silva A, Souza Filho I R, Lu W, Zilnyk K D, Hupalo M F, Alves L M, Ponge D, Gault B and Raabe D 2022 A sustainable ultra-high strength Fe18Mn3Ti maraging steel through controlled solute segregation and α-Mn nanoprecipitation *Nat. Commun.* **13** 2330
[29] Wang H *et al* 2020 Effect of cyclic rapid thermal loadings on the microstructural evolution of a CrMnFeCoNi high-entropy alloy manufactured by selective laser melting *Acta Mater.* **196** 609–25
[30] Zeisl S, Lassnig A, Hohenwarter A and Mendez-Martin F 2022 Precipitation behavior of a Co-free Fe-Ni-Cr-Mo-Ti-Al maraging steel after severe plastic deformation *Mater. Sci. Eng.* A **833** 142416
[31] Schnitzer R, Schober M, Zinner S and Leitner H 2010 Effect of Cu on the evolution of precipitation in an Fe-Cr-Ni-Al-Ti maraging steel *Acta Mater.* **58** 3733–41
[32] Jägle E A, Sheng Z D, Kürnsteiner P, Ocylok S, Weisheit A and Raabe D 2017 Comparison of maraging steel micro- and nanostructure produced conventionally and by laser additive manufacturing *Materials* **10** 8
[33] Zhang Y N, Cao X, Wanjara P and Medraj M 2013 Oxide films in laser additive manufactured Inconel 718 *Acta Mater.* **61** 6562–76
[34] Meng F J, Wang J Q, Han E H and Ke W 2010 The role of TiN inclusions in stress corrosion crack initiation for alloy 690TT in high-temperature and high-pressure water *Corros. Sci.* **52** 927–32
[35] Zhang S Y, Wang L L, Lin X, Yang H O and Huang W D 2022 The formation and dissolution mechanisms of Laves phase in Inconel 718 fabricated by selective laser melting compared to directed energy deposition and cast *Composites* B **239** 109994
[36] Tan C L, Zou J, Wang D, Ma W Y and Zhou K S 2022 Duplex strengthening via SiC addition and in-situ precipitation in additively manufactured composite materials *Composites* B **236** 109820
[37] Wang Y H, Kang J M, Peng Y, Wang T S, Hansen N and Huang X 2018 Hall-Petch strengthening in Fe-34.5Mn-0.04C steel cold-rolled, partially recrystallized and fully recrystallized *Scr. Mater.* **155** 41–45
[38] Yin Y, Tan Q Y, Bermingham M, Mo N, Zhang J Q and Zhang M X 2022 Laser additive manufacturing of steels *Int. Mater. Rev.* **67** 487–573
[39] Tan C L, Chew Y, Weng F, Sui S, Du Z L, Ng F L and Bi G J 2021 Superior strength-ductility in laser aided additive manufactured high-strength steel by combination of intrinsic tempering and heat treatment *Virtual Phys. Prototyp.* **16** 460–80
[40] Lewandowski J J and Seifi M 2016 Metal additive manufacturing: a review of mechanical properties *Annu. Rev. Mater. Res.* **46** 151–86
[41] Niu H, Jiang H C, Zhao M J and Rong L J 2021 Effect of interlayer addition on microstructure and mechanical properties of NiTi/stainless steel joint by electron beam welding *J. Mater. Sci. Technol.* **61** 16–24
[42] Bleck W, Guo X F and Ma Y 2017 The TRIP effect and its application in cold formable sheet steels *Steel Res. Int.* **88** 1700218
[43] Zhu Y T *et al* 2021 Heterostructured materials: superior properties from hetero-zone interaction *Mater. Res. Lett.* **9** 1–31